SAND86-9009
Unlimited Release
Printed January 1987

SAND--86-9009

DE88 010499

Oxidation and Chromium Depletion of Alloy 800 and 316SS by Molten $NaNO_3$-KNO_3 at Temperatures Above 600°C

R. W. Bradshaw

Prepared by
Sandia National Laboratories
Albuquerque, New Mexico 87185 and Livermore, California 94550
for the United States Department of Energy
under Contract DE-AC04-76DP00789

Issued by Sandia National Laboratories, operated for the United States Department of Energy by Sandia Corporation.

SAND86-9009
Unlimited Release
Printed January 1987

OXIDATION AND CHROMIUM DEPLETION OF ALLOY 800 AND 316SS BY MOLTEN $NaNO_3$-KNO_3 AT TEMPERATURES ABOVE 600°C

Robert W. Bradshaw
Exploratory Chemistry Division I
Sandia National Laboratories Livermore

Abstract

The corrosion behavior of Alloy 800 and Type 316 stainless steel in molten $NaNO_3$-KNO_3 was studied at temperatures from 605°C to 630°C. Corrosion behavior was significantly different from that previously reported in nitrate melts at temperatures up to 600°C and involved a combination of oxidation, internal nitridation and sodium metallate formation. Corrosion kinetics, determined metallographically, switched from a parabolic to a linear rate equation as temperature increased. Corrosion was uniform and resulted in metal losses on the order of 100 microns/year at 630°C. Among the alloying elements, chromium was depleted from the alloy as the result of a basic fluxing process. The kinetic equations describing chromium depletion also changed from parabolic to linear with increasing temperature. The effect of the equilibrium chemistry of the melt on the corrosion behavior of the alloys is analyzed and possible corrosion mechanisms are discussed.

Acknowledgments

Some of these results were presented at the 168th Electrochemical Society Meeting, Las Vegas, NV, at the Symposium on High Temperature Materials Chemistry-III on Oct. 16, 1985. A condensed version of this report will appear in a Proceedings volume in press.

The author would like to acknowledge the efforts of C. W. Karfs, 8316, in conducting the electron microprobe analysis and A. D. Gardea, 8316, in preparing the metallographic specimens.

Solar Thermal Technology Foreword

The research and development described in this document were conducted within the Solar Thermal Technology Program of the U. S. Department of Energy (DOE). The goal of the Solar Thermal Technology Program is to advance the engineering and scientific understanding of solar thermal technology and to establish the technology base from which private industry can develop solar thermal power production options for introduction into the competitive energy market.

Solar thermal technology concentrates solar radiation by means of tracking mirrors or lenses onto a receiver where the solar energy is absorbed as heat and converted into electricity or incorporated into products as process heat. The two primary solar thermal technologies, central receivers and distributed receivers, employ various point and line-focus optics to concentrate sunlight. Current central receiver systems use fields of heliostats (two-axis tracking mirrors) to focus the sun's radiant energy onto a single tower-mounted receiver. Parabolic dishes up to 17 meters in diameter track the sun in two axes and use mirrors or Fresnel lenses to focus radiant energy onto a receiver. Troughs and bowls are line-focus tracking reflectors that concentrate sunlight onto receiver tubes along their focal lines. Concentrating collector modules can be used alone or in a multi-module system. The concentrated radiant energy absorbed by the solar thermal receiver is transported to the conversion process by a circulating working fluid. Receiver temperatures range from 100°C in low-temperature troughs to over 1500°C in dish and central receiver systems.

The Solar Thermal Technology Program is directing efforts to advance and improve promising system concepts through the research and development of solar thermal materials, components, and subsystems, and the testing and performance evaluation of subsystems and systems. These efforts are carried out through the technical direction of DOE and its network of national laboratories who work with private industry. Together they have established a comprehensive goal directed program to improve performance and provide technically proven options for eventual incorporation into the nation's energy supply.

To be successful in contributing to an adequate national energy supply at reasonable cost, solar thermal energy must eventually be economically competitive with a variety of other energy sources. Components and system-level performance targets have been developed as quantitative program goals. The performance targets are used in planning research and development activities, measuring progress, assessing alternative technology options, and making optimal component developments. These targets will be pursued vigorously to ensure a successful program.

The work described in this report concerns a study of the corrosion behavior of high-temperature alloys by molten salts and addresses the program sub-element concerning molten salt solar central receiver technology development. These alloys are intended as materials of construction of several major subsystems of solar central receivers, such as the receiver tubes, superheater and high-temperature salt transfer lines. The main objective of the work was to determine the temperature limitations imposed by corrosion on metallic containment materials, such as Alloy 800 and 316SS, and to analyze the corrosion mechanisms.

Contents

Illustrations

Tables

OXIDATION AND CHROMIUM DEPLETION OF ALLOY 800 AND 316SS BY MOLTEN $NaNO_3$-KNO_3 AT TEMPERATURES ABOVE 600°C

Introduction

The use of a molten alkali nitrate salt mixture as a heat transfer and storage fluid in solar central receiver (SCR) systems has created an interest in the corrosion behavior of containment alloys at temperatures significantly higher than those encountered in well established industrial uses of such salts [1]. In SCR systems, temperatures are expected to reach 600°C at some locations on the absorber tubes [2] and might possibly exceed this value. Previous studies of corrosion in this laboratory, using thermal convection loops, demonstrated an apparent transition from slow to rapid corrosion at about 600°C for several iron-nickel-chromium alloys [3]. In view of these preliminary results, more information concerning corrosion of these alloys in molten salt at high temperatures was desirable to predict reliability.

Relatively little data have been reported concerning corrosion of Fe-Ni-Cr alloys in molten nitrates at temperatures above 600°C. Tortorelli and DeVan conducted thermal convection loop experiments with Alloy 800 and 316SS, using argon as a cover gas, and reported a sharp increase in the concentration of a soluble chromium species in the melts when the maximum temperature was increased from 600°C to 625°C [4]. X-ray diffraction of Alloy 800 and 316SS immersed in melts at 630°C indicated the formation of sodium ferrate, among several other products [5]. Slusser and co-workers recently examined a number of alloys in molten nitrates at temperatures from 650°C to 700°C and observed rapid corrosion [6]. Inspection of some metallic components from a reactor using molten nitrate salt at various temperatures above 650°C also revealed rather severe corrosion [7].

Above 600°C, the thermodynamic equilibria of several decomposition reactions intrinsic to alkali nitrates favor the formation of significant

amounts of other ionic species. The dissociation reaction of nitrate ion, to form nitrite ion and oxygen,

$$(1) \qquad NO_3^{-1} = NO_2^{-1} + 1/2\ O_2$$

favors the formation of nitrite as temperature increases [8]. At 630°C, the molar ratio of nitrite to nitrate in a melt equilibrated with one atmosphere of oxygen is approximately 0.1 [8]. Other reactions involving nitrate or nitrite ions can produce several oxide ion species, of which peroxide, O_2^{-2}, is the most stable [9]. Thermodynamic calculations have indicated that the peroxide ion content could reach one mole percent at 630°C [9]. Since oxide ions are particularily aggressive in a variety of molten salt environments [10], it seems likely that chemical changes in nitrate melts could accelerate corrosion at temperatures above 600°C.

The purpose of this study was to examine the corrosion behavior of Alloy 800 and 316SS in molten $NaNO_3$-KNO_3 over the temperature range of 605°C to 630°C. The approach was to conduct long-term exposure tests and apply metallographic, electron optic and X-ray analyses to identify the corrosion products. The depletion of chromium from the alloy as a soluble corrosion product was also studied to provide additional insight into the corrosion process. Particular emphasis was placed on determining the kinetics of alloy oxidation and elemental depletion and applying thermochemical analysis to understand the behavior of alloys in this environment.

Experimental Methods

Corrosion tests were conducted by immersing alloy coupons in melts of reagent grade $NaNO_3$-KNO_3, 1:1 molar ratio, at temperatures of 605°C, 615°C, and 630°C for several thousand hours. The melts for each type of alloy were contained in high-purity alumina tubes (McDanel Refractory Co., Beaver Falls, PA) that were heated in crucible furnaces. The tubes were not sealed, which allowed the salt to equilibrate with the atmosphere. Coupons were withdrawn periodically, weighed after removal of residual salt by ultrasonic rinsing in hot water, and returned to the crucibles. Dissolved

alloying elements were determined by periodically withdrawing salt samples from each melt, quenching them and analyzing for transition metal content by atomic absorption spectroscopy.

The elemental compositions of the Alloy 800 and 316SS specimens used in these experiments are given in Table I. Coupons (25mm x 9mm x 1.5mm) were fabricated from sheet stock (Metal Samples, Inc., Munford, AL) and were ground with 180 SiC paper and rinsed in isopropanol before immersion. At various intervals, samples were prepared for metallographic examination by optical and scanning electron microscopy. Corrosion product phases were identified by electron microprobe analysis and X-ray diffraction, using sequential sectioning to obtain depth profiles in several cases [5]. Electron microprobe analysis was used to supplement X-ray diffraction by determining the thickness of the oxide and depletion layers and identifying solid solution phases. Electron microprobe analyses were performed with a JEOL Superprobe 733 using Fe_2O_3 as an oxygen standard and pure elements as the metallic standards.

Results and Discussion

Effect of Temperature on Solid Oxidation Products

Both alloys corroded uniformly at the three temperatures studied and the corrosion products were generally adherent, which permitted them to be examined by standard metallographic methods. The corrosion product morphologies observed on Alloy 800 at the end of each experiment are shown in the micrographs of cross-sectioned coupons in Figure 1. The corrosion products identified by X-ray diffraction and electron microprobe analyses at each temperature are indicated.

At 605°C, the corrosion products formed on Alloy 800 (see Figure 1a) consisted of an outer layer of magnetite (Fe_3O_4) and sublayers of several mixed oxides. These included an M_3O_4-spinel, composed mostly of Fe, but containing significant amounts of Cr and Ni, and a M_2O_3-type oxide enriched in Cr, but containing Ni and Fe as well. After 4111 hours, approximately 15

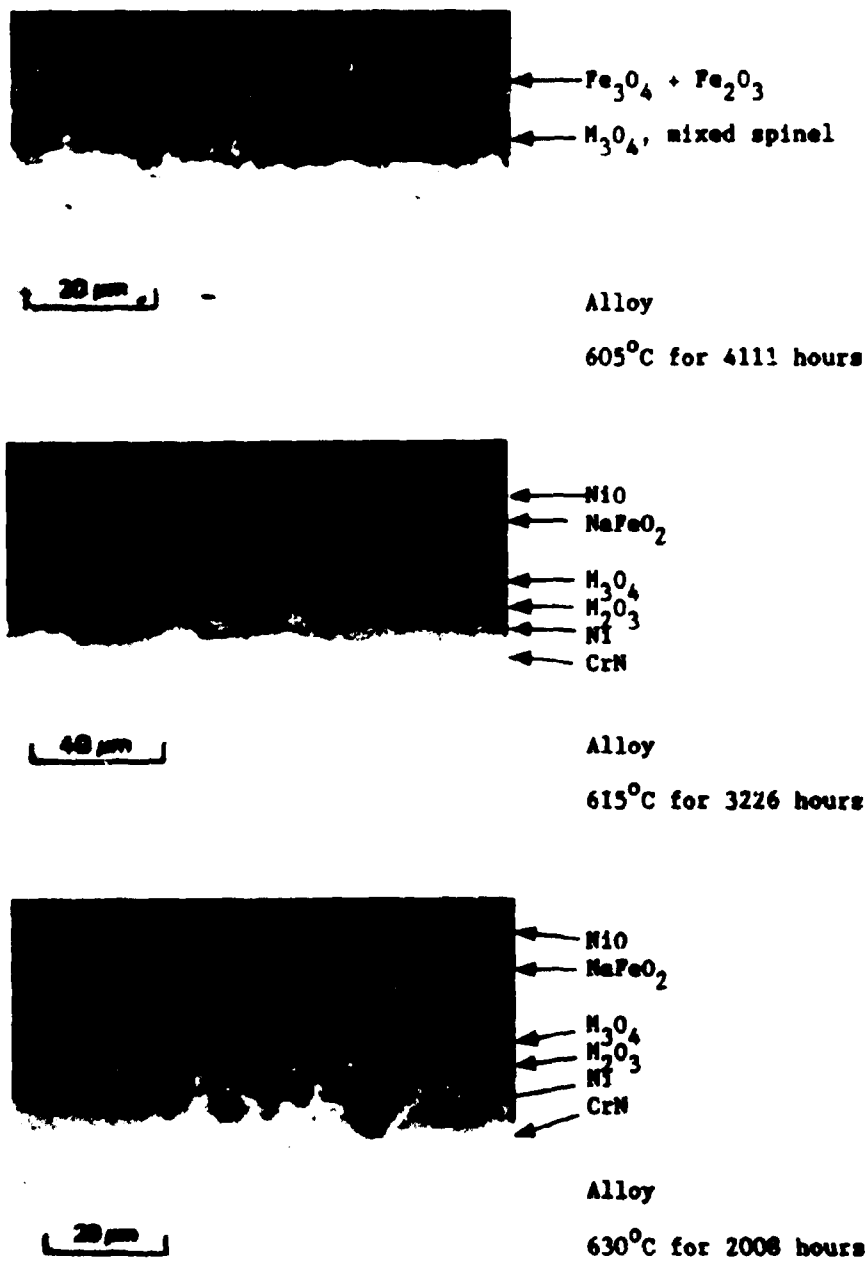

Figure 1. Photomicrographs of corrosion products on Alloy 800 after immersion in molten $NaNO_3$-KNO_3. The temperature and duration of each test are noted and the phase identifications are given.

microns of oxide scale had formed. The elemental concentration profiles of the surface layers obtained by electron microprobe analysis (EMPA) are shown in Figure 2. The correspondence between position in the microprobe scan and the product layers identified in Figure 1a are indicated at the top. Several features are worth noting. First, chromium was absent from the outer oxide layer, which was in contact with the melt. Since Cr was found as a solute in the melt, as discussed later, it must diffuse through the outer Fe_3O_4 layer readily. Second, an oxide layer composed solely of Cr did not form, which reduced the ability of the alloy to protect itself. Lastly, a metallic segregation zone formed beneath the oxidation products, in which Fe and Cr were depleted and Ni was enriched.

At 615°C and 630°C, scaling was much more rapid and the composition of the oxidation products changed substantially. Alloy 800 formed corrosion product layers which were 32 microns thick after 2008 hours at 630°C and 43 microns thick after 3226 hours at 615°C. Corrosion product morphologies at these temperatures were rather complex, as shown in Figure 1b and c. Starting at the interface in contact with the melt and proceeding inward, the oxidation products on Alloy 800 consisted of layers of sodium ferrate ($NaFeO_2$), iron-chromium spinels (M_3O_4 type) and chromium-rich M_2O_3 oxides. Below the oxide layers, internal nitridation had precipitated a band of chromium nitride, along with some titanium nitride, and a metallic layer enriched in nickel and depleted in iron and chromium. Isolated crystallites of NiO, which appear as small white particles in the micrographs, were observed at the salt-contacting interface of the $NaFeO_2$ layer. More NiO may have been deposited at the surface of the $NaFeO_2$ layer than was retained during the metallographic preparation procedure.

The concentration profiles determined by EMPA (see Figure 3) illustrate the distribution of alloying (Fe, Ni, Cr) and environmental (O, Na, N) elements in the corrosion products on Alloy 800 after exposure at 630°C. The correspondence between position in the microprobe scan and the product layers noted in Figure 1c are indicated at the top. It is evident that the layers in the scale are solid solution oxides, rather than the pure compounds, except for $NaFeO_2$. The presence of NiO crystals at the surface in contact with the molten salt (see Figure 1c) was confirmed by the abrupt

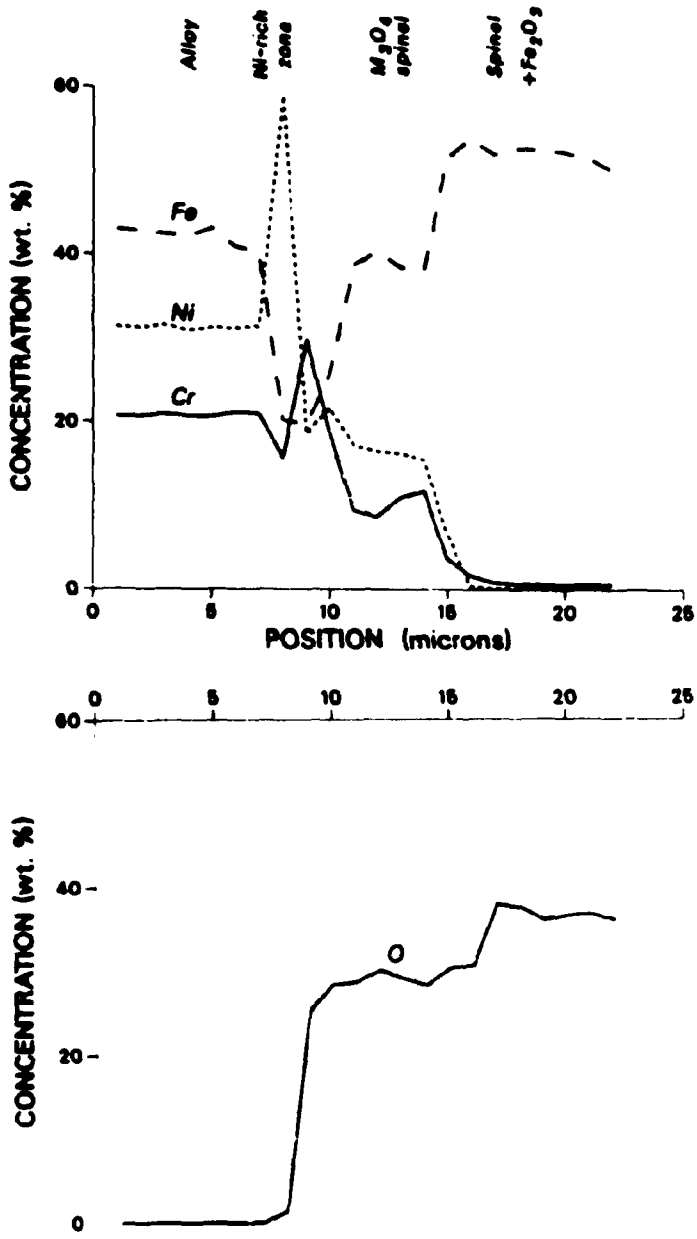

Figure 2. Electron microprobe analysis of Alloy 800 after 4111 hours in a nitrate melt at 605°C. The distribution of the alloying elements and oxygen among the corrosion products may be compared with the morphology indicated in Fig. 1.

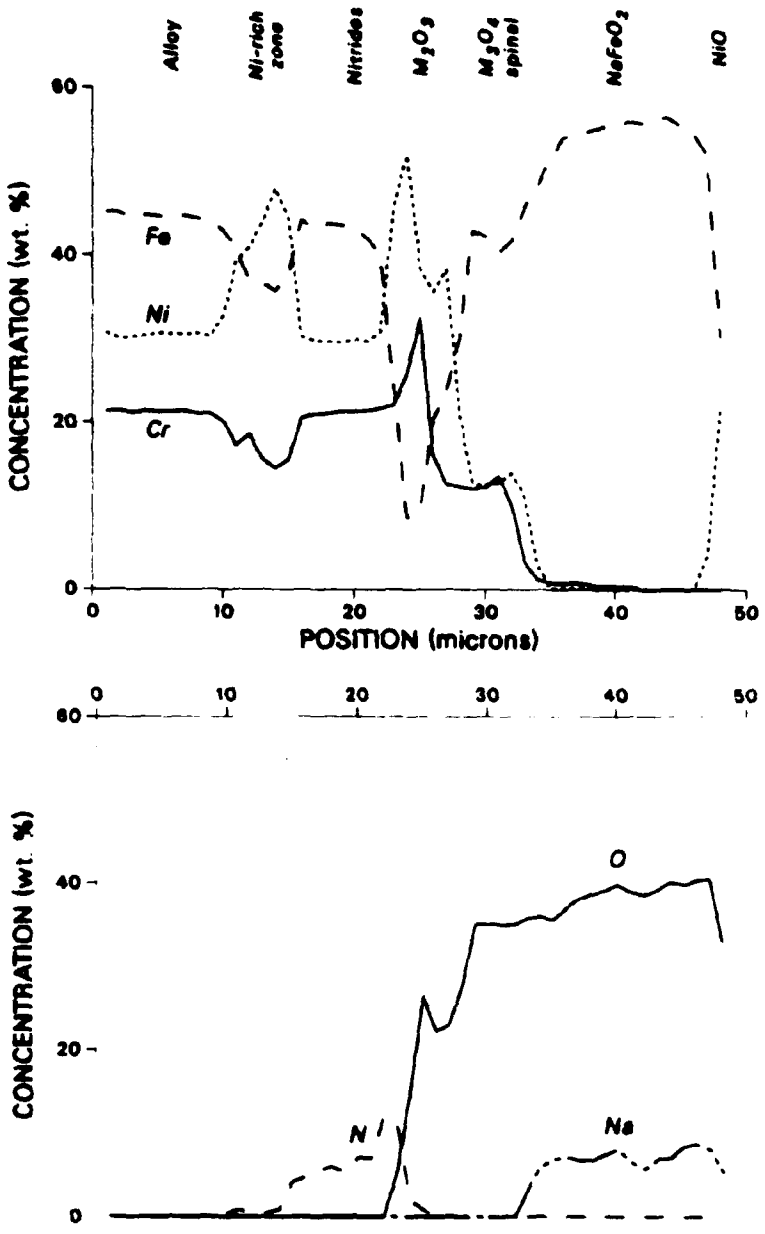

Figure 3. Electron microprobe analysis of Alloy 800 after 2008 hours in a nitrate melt at 630°C. The distribution of the alloying elements and oxygen among the corrosion products may be compared with the morphology indicated in Fig. 1.

rise in the nickel profile at the position, 48 microns. The presence of a metallic segregation zone, where Ni was substantially enriched, can be discerned as can a band of internal nitrides formed beneath the oxide layers.

The effect of temperature on both the identity of the corrosion products and the extent of corrosion of 316SS was analogous to Alloy 800; although some qualitative differences were observed. The structure of the oxide scales on 316SS were less complicated than Alloy 800 and were not as well differentiated, particularly after long periods of immersion at 615°C and 630°C. The micrographs of cross-sectioned coupons and the corresponding oxidation products identifications at various temperatures are shown in Figure 4. The formation of $NaFeO_2$ at 615°C and 630°C is evident from Figures 4b and 4c. It was also observed that the scale on 316SS tended to form voids and blisters, which were not observed on Alloy 800, and was also less adherent. Internal nitrides were found, but these were less obvious in 316SS at 615°C and 630°C. Morphological features related to the Ni content of the alloy, including the Ni enrichment zone beneath the surface scale and the NiO crystallites in the $NaFeO_2$ layer, were less pronounced than with Alloy 800.

Soluble Corrosion Products

Chromium was lost from the alloy by dissolution in the melt, as well as by oxide scale formation. The presence of dissolved Cr was visually evident from the increasingly bright yellow color of the melts as the tests progressed. Chemical analysis of quenched samples of the melt for alloying elements revealed only chromium in detectable quantities; neither iron nor nickel appeared to be soluble. This agrees with other observations at comparable temperatures [3,4,5].

Although the identity of the chromium-containing species was not determined in the molten salt, a number of observations suggest that chromate ion, CrO_4^{-2}, was the most abundant form. The yellow color is consistent with the presence of chromate, rather than dichromate, which

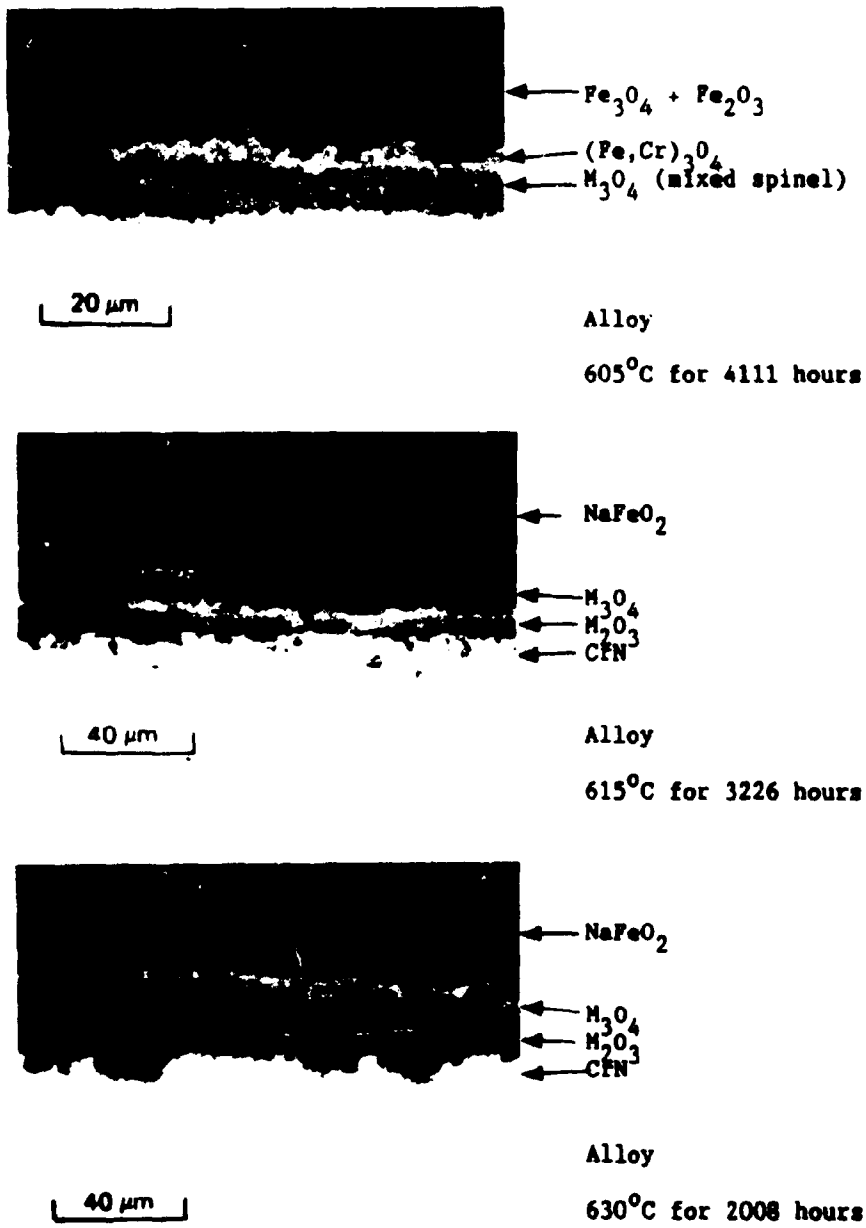

Figure 4. Photomicrographs of corrosion products on 316SS after immersion in molten $NaNO_3$-KNO_3. The temperature and duration of each test are noted and the phase identifications are given.

yields an orange color [11]. Also, polarographic analysis of samples dissolved in water identified chromate ion.

That chromate was the soluble Cr species in these tests is also supported by other investigations. Chemical analysis of aqueous solutions of quenched salt samples from a thermal convection loop identified primarily hexavalent Cr and a minor amount of the trivalent form [4]. Trivalent chromium and chromium metal were reported to oxidize to hexavalent chromium in $LiNO_3$-KNO_3 at 300°C [12]. Upon heating above 350°C, dichromate, $Cr_2O_7^{-2}$, was oxidized to chromate [12]. Several other studies have reported that dichromate was converted to chromate in equimolar $NaNO_3$-KNO_3 at temperatures from 250°C to 300°C [13-15]. At 550°C, an equimolar $NaNO_3$-KNO_3 melt initially containing dichromate produced the yellow color associated with chromate after several hours [11].

Based upon the above results and previous observations, it is almost certain that chromium dissolves in molten nitrate salt as chromate. Since the solubility of Cr, as chromate (or dichromate), would exceed 10 mole percent at all temperatures of interest in central solar receiver systems [16], the kinetics and mechanisms which influence Cr depletion are of obvious interest. Some aspects of the thermochemistry and corrosion kinetics which influence chromium depletion are discussed below.

Thermochemical Analysis

Thermochemical stability calculations can be quite helpful for understanding corrosion behavior in high temperature environments in which many oxidation products are formed. Thermodynamic analysis can clarify some of the observations described in the two preceding sections, including the morphology of oxidation products observed on the alloys. The phase stability behavior of Fe-Ni-Cr alloys in molten nitrate salt can be described by considering two limiting cases, the stability of the metallic oxidation products of the alloys in a sodium-free environment of oxygen and nitrogen and the equilibria between the relevant metal oxides and molten nitrate salt.

The phase stability diagrams for Fe, Ni and Cr in oxygen and nitrogen activity coordinates were constructed for a temperature of 627°C (900 K), using free energy data from Barin and Knacke [17]. The metallic elements and their oxidation products were assumed to be at unit activity and the resulting diagrams were superimposed on one another as shown in Figure 5. The corrosion products of interest are those which are stable in the region below and to the left of the cross which marks the thermodynamic activity of air, the cover gas used in these experiments. CrN was the only stable nitride phase and forms only at very low oxygen activity, as might be encountered beneath surface oxide layers. The shift in the phase stability boundary of CrN as temperature decreases cannot account for its absence at 605°C (see Figure 1). The absence of CrN at 605°C must be due to a kinetic effect resulting from the formation of protective surface layers.

For alloys which form solid solution oxides, simplified diagrams such as Figure 5 may not necessarily represent the correct ordering of the possible phases. This point has been discussed by Whittle [18] and others. This appears to be the case here, with respect to the position of the M_2O_3 oxide layer. However, since sufficient data are not available to construct a rigorous diagram, the simplified diagram is still useful as a convenient means to enumerate some of the possible oxidation products.

The calculations supporting Figure 5 assumed that no alkali nitrate was present. At the surface of the corrosion layer, and within if the scale is microscopically porous, the equilibria between the oxide phases in Figure 5 and the molten salt must also be considered. Before discussing that point, briefly consider the equilibria of molten alkali nitrate salt and its decomposition products. The intrinsic equilibria of the molten salt depends on the local oxygen and nitrogen activities and temperature. Calculations of this equilibria have been made by Nagelberg and Mar, using the simplifying assumption that the melt was solely $NaNO_3$ [9]. Their approach was used here to compute the phase stability boundaries of sodium nitrate and its decomposition products at 900K (627°C), sodium nitrite, peroxide and oxide, using available free energy data [9,17]. Ideal behavior and complete miscibility were assumed. The calculated phase boundaries, which represent equal activities of each compound, are given by the solid

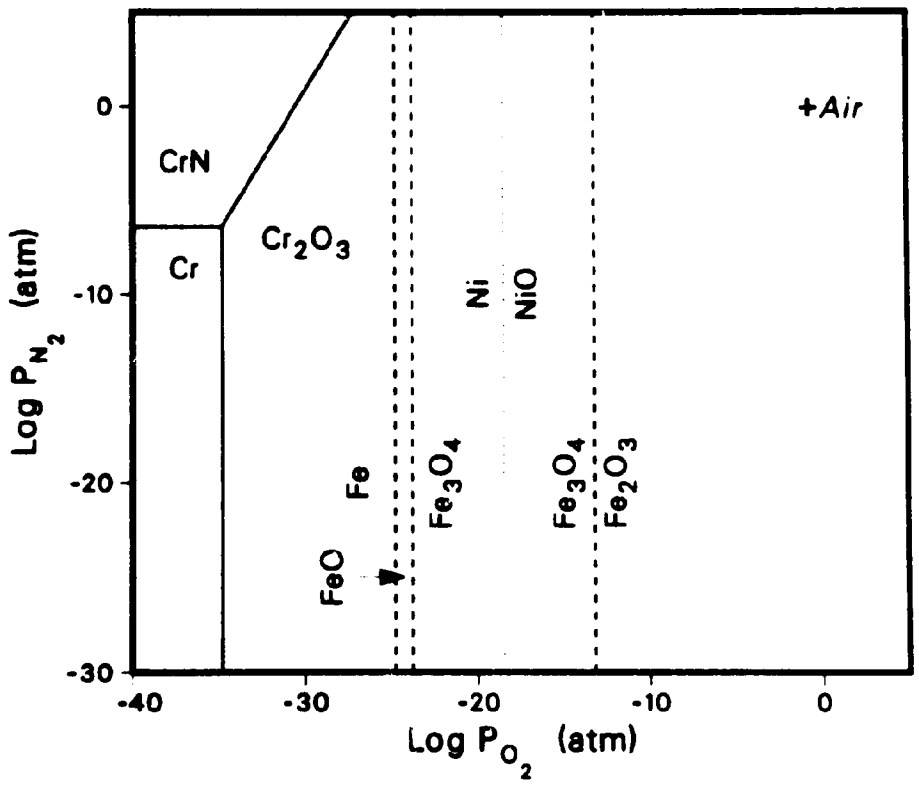

Figure 5. Superimposed thermodynamic stability diagrams for Fe, Ni and Cr with oxygen and nitrogen at 900K (627°C). The dashed lines refer to Fe phases, the dotted to Ni and the solid to Cr.

lines in Figure 6. The phases of interest again lie below and to the left of the cross which marks the coordinates of the cover gas, air. It is apparent that, while nitrate is stable in air, the boundary with peroxide lies quite close. As Nagelberg and Mar have calculated, the concentration of peroxide increases rapidly as temperature increases in the range of interest here [9].

The interaction between the molten salt and oxides of alloying elements can form several sodium-metal-oxides, according to the reactions written below.

(2) $Fe_2O_3 + 2\ NaNO_3 = 2\ NaFeO_2 + 5/2\ O_2 + N_2$

(3) $NiO + 2\ NaNO_3 = Na_2NiO_2 + 5/2\ O_2 + N_2$

(4) $Cr_2O_3 + 2\ NaNO_3 = 2\ NaCrO_2 + 5/2\ O_2 + N_2$

Sodium chromite (Eqn. 4) is a metastable product in this environment, however, and is superseded by formation of sodium chromate,

(5) $Cr_2O_3 + 4\ NaNO_3 = 2\ Na_2CrO_4 + 7/2\ O_2 + 2\ N_2$

The phase stability boundaries of the metal oxides and sodium metallates in Equations (2)-(5) were calculated using published data on free energy changes [17,19], assuming that the solid products and $NaNO_3$ were at unit activity. The boundaries are shown by the dotted lines in Figure 6 and are superimposed on the equilibrium diagram of the molten salt. Note that the phase stability field for sodium chromate encompasses virtually the entire diagram.

It is evident from Figure 6 that the stable phases of the alloying elements in contact with the melt in equilibrium with air are $NaFeO_2$, NiO and Na_2CrO_4. The successive layering of metallic oxides and internal nitride determined by metallographic analysis at 615°C and 630°C is consistent with paths on the stability diagrams which proceed from the activity of air to the very low activity of oxygen and nitrogen which must

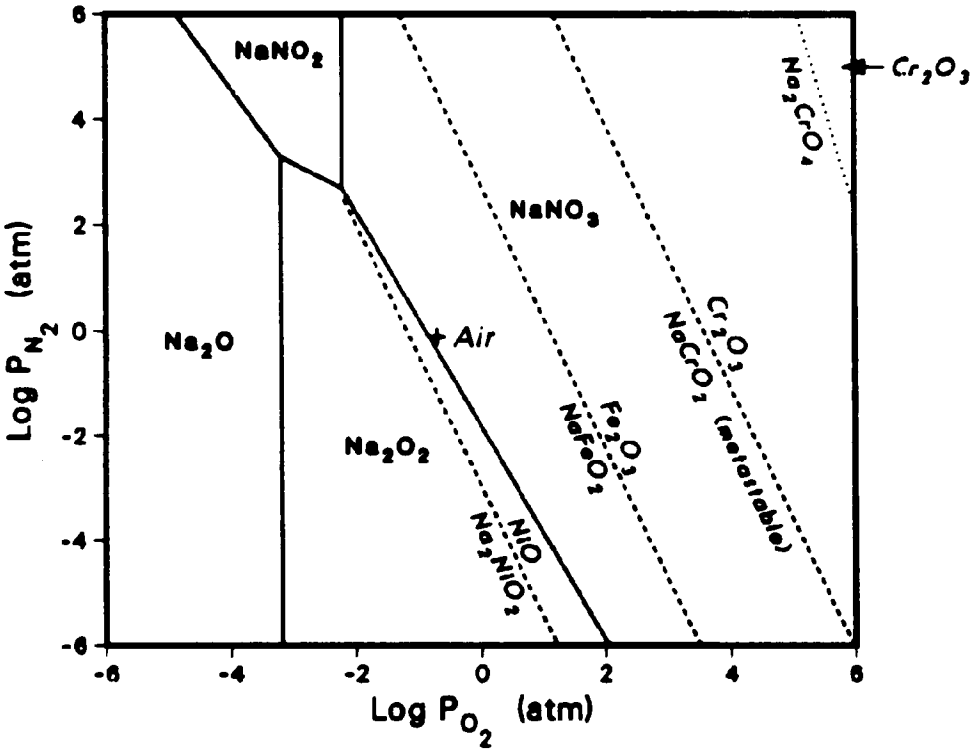

Figure 6. Phase stability diagram for the Na-O-N system at 900K (solid lines). The phase stability boundaries between the oxides of Fe, Ni and Cr and their respective compound oxides with sodium are given by the dotted lines.

obtain within the unaffected alloy. Such a path would start on Fig. 6, then transfer to Fig. 5 at a point beneath the $NaFeO_2$ layer where the activity of $NaNO_3$ must become very low.

All of the phase stability boundaries shown in Figs. 5 and 6 shift to lower values of oxygen activity as temperature decreases. However, the magnitude of this shift is not sufficient to account for the absence of $NaFeO_2$ at 605°C. A likely cause is that the kinetics of the conversion of magnetite and hematite to $NaFeO_2$ is slow, due to the low concentration of peroxide ion in the melt at this temperature.

Oxidation Kinetics

Although gravimetric measurements are commonly used to determine the kinetics of corrosion, this approach was unsuitable here. Weight change was not stoichiometrically related to the amount of metal consumed because of the type of corrosion products formed. This is evident from the results on corrosion products described above, which incorporate O, Na and N from the environment. Additional factors which complicated the interpretation of weight change data were chromium depletion and oxide spallation.

Since Alloy 800 and 316SS corroded by uniform scale formation, kinetic data were obtained by measuring scale thickness. This method assumes that scale thickness is directly proportional to the amount of metal which reacted with the environment. Minor errors will arise when multiple products are formed, particularly if the density of the alloying elements differs significantly among the corrosion products, as between $NaFeO_2$ and the various transition metal oxides. The presence of a dispersed corrosion product, CrN, creates another difficulty in quantification.

The thicknesses of surface scales were measured from photomicrographs of metallographically-prepared coupons after various periods of immersion in the melts. Although the number of data points was limited by practical considerations, trends in corrosion kinetics were revealed clearly and consistently. The data relating oxide thickness to time are shown in the

log-log plots in Figure 7 for Alloy 800 (a) and 316SS (b). At 615°C and 630°C, a slope of one provided the best fit for both alloys, indicating linear scale growth with time. Linear metal loss kinetics have also been observed by Slusser, et al, at temperatures above 650°C [6]. At 605°C, Alloy 800 displayed parabolic kinetics (slope = 0.5), while 316SS followed parabolic kinetics for about 2000 hours and then showed a systematically increasing slope as time increased.

The data given in Figure 7 were used to calculate annual metal losses by extrapolating to 8760 hours (1 year) and converting from scale thickness to equivalent metal loss. These values appear in Table II, along with data from other studies conducted at temperatures which bracket those reported here. The values of metal losses below 615°C were calculated using a parabolic rate law, while a linear equation was used at higher temperature. To provide a common basis for comparison, losses for the first year are given for temperatures below 615°C. Metal losses corresponding to the lifetime of an SCR would have to be extrapolated appropriately.

At temperatures of 600°C and below, corrosion rates were nominally less than 10 microns/year. The data obtained here showed a substantial increase in the corrosion rate as temperature increased above 600°C, as shown in Table II. Based on scale thickness measurements, metal losses of 75-100 microns/year (3-4 mils/year) are expected for Alloy 800 and 316SS at 630°C. The metal loss of 316SS at 630°C was also determined by chemical descaling, using a method described previously [20], and a value of 86 microns/year was obtained, which compares well with the value estimated from scale thickness. The data at 650°C reported by Slusser [6] agree well with the trend observed in this study. The extremely high corrosion rates reported at 677°C were probably caused by substantial decomposition of the salt, which would yield high oxide ion concentrations.

Chromium Depletion Kinetics

The solubility of chromium in the melt allowed measurements to be made of the cumulative flux of Cr through the corrosion product layer. Although

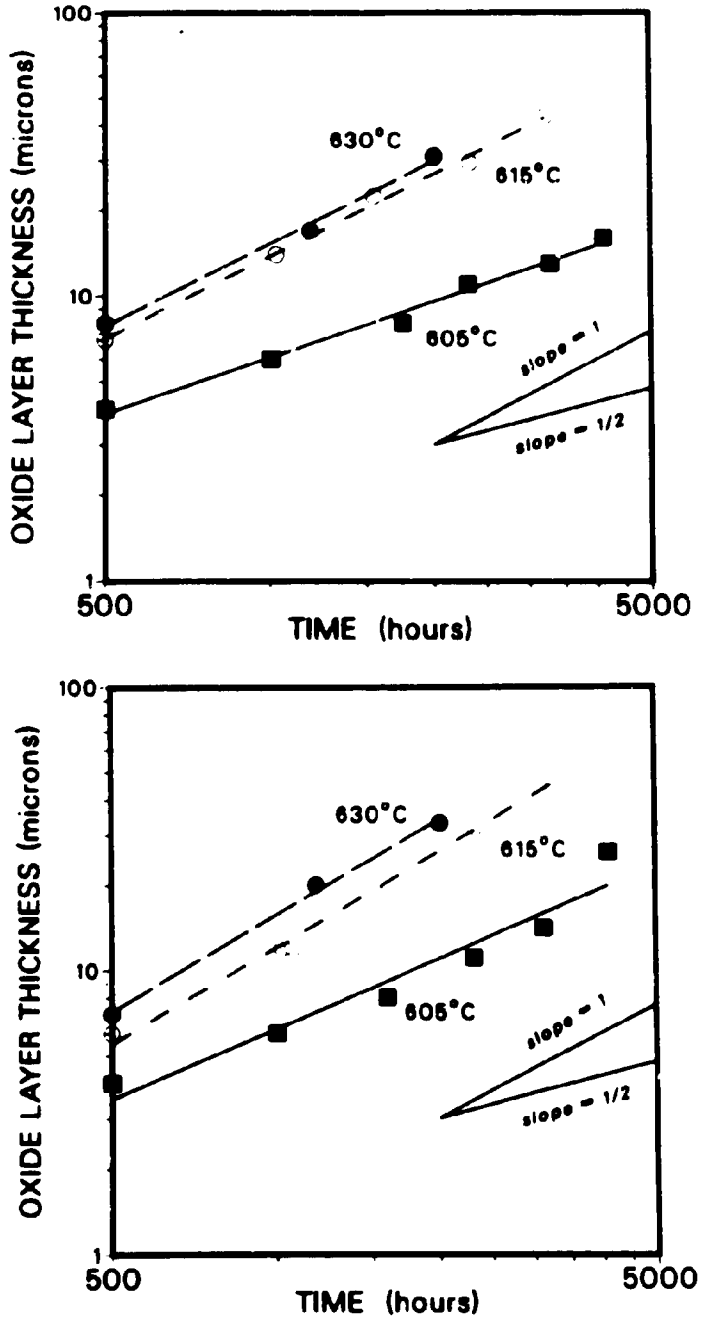

Figure 7. The growth of oxide scales with time, plotted in log-log coordinates, for (a) Alloy 800 and (b) 316SS in molten $NaNO_3$-KNO_3. The trends in the data are linear at 615°C and 630°C and approximately parabolic at 605°C.

TABLE I.

ELEMENTAL COMPOSITION OF ALLOYS TESTED
(WEIGHT PERCENT; BALANCE Fe)

Alloy	Cr	Ni	C	Other
Alloy 800 (by analysis)	20.7	31.0	.02	.44 Al .45 Ti .57 Cu
316SS (nominal)	16-18	10-14	.08max	2-3 Mo

TABLE II

METAL LOSS RATES OF ALLOY 800 AND 316SS IN MOLTEN NITRATE SALT OVER A RANGE OF TEMPERATURES

Temperature (°C)	Source of Data	Alloy 800 (microns/yr)	316SS (microns/yr)
565*	Ref. 18	5.4	--
595*	"	7.5	--
595*	Ref. 4	5.7	3.6
600*	"	5. 7	7.2
605*	This study	17	26
615	" "	66	82
630	" "	75	106
630**	" "	--	86
650	Ref. 6	107	165
677	"	1040	2060

* The values of metal losses above 605°C are based on linear kinetics. A parabolic rate law was used at temperatures up to 605°C, for which losses during the first year are given for comparison.

** Determined by measuring descaled weight loss.

measurements of this kind do not appear to have been made previously in molten salt corrosion experiments, they provide very useful information on the kinetics of chromium depletion, as well as insight into the corrosion process. The concentration of chromium in the melts containing Alloy 800 and 316SS was measured periodically and the data were converted to the equivalent coupon weight loss, in units of mg/cm2, given the surface area of the coupons and the mass of molten salt in the crucible. Chromium weight loss can be related to the affected depth in an alloy by noting that a loss of 1 mg/cm2 corresponds to depletion of a band about 6 microns thick for an alloy containing 20 wt.% Cr. The Cr weight loss results are plotted versus time in Figure 8. The weight losses shown in these plots can be treated in the same manner as weight gains in corrosion experiments when analyzing the kinetics of chromium depletion. A qualitative interpretation is appropriate given the amount of data available.

The general features of the kinetics of chromium depletion of Alloy 800 and 316SS were similar, although the Cr loss from Alloy 800 was somewhat less than from 316SS, despite the lower Cr content of the latter. Chromium losses increased monotonically with time, suggesting a power-law interpretation typically applied to oxidation kinetics. At 605°C, the equation providing the best fit for both Alloy 800 and 316SS was a square root dependence on time (parabolic). At 615°C and 630°C, a linear equation was best for 316SS. Alloy 800 was also linear at 630°C, but a slight deviation from a slope of unity was apparent at 615°C. The net amount of chromium lost at 605°C was substantially less than at higher temperatures, where chromium losses approaching 2 mg/cm2 were observed.

The ability to acquire quantitative data on Cr depletion provided a novel means of investigating the corrosion behavior of these alloys in molten nitrate salt. The transition from parabolic to linear kinetics of Cr depletion with increasing temperature mimiced that observed in the growth of surface oxide layers and suggests a common basis for the two processes. In the next section, several aspects of the corrosion mechanism will be discussed in view of the kinetic results and the thermochemical analysis.

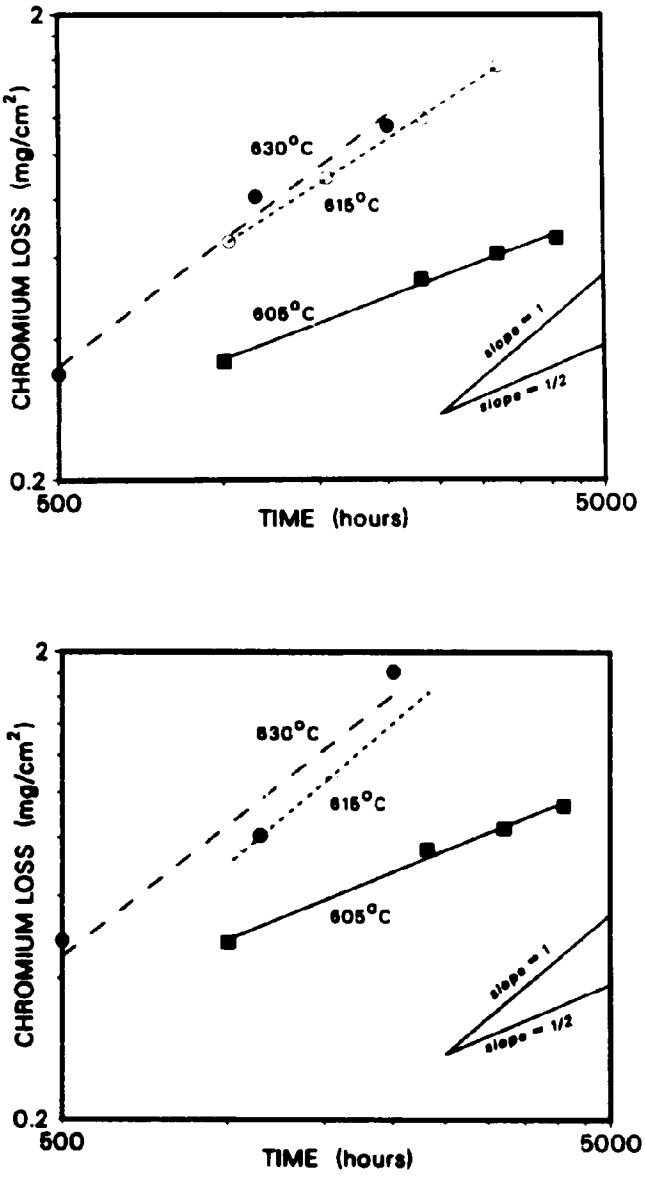

Figure 8. Kinetic trends of Cr depletion from (a) Alloy 800 and (b) 316SS, as determined from Cr dissolved in the melt, plotted in log-log coordinates. The data imply linear kinetics at 615°C and 630°C and parabolic kinetics at 605°C.

Corrosion and Mass Transport Mechanisms

The most straightforward interpretation of the parabolic rate equations determined for both alloys at 605°C is that a protective layer was formed, whose growth rate was limited by diffusion [21]. Linear corrosion kinetics are typically ascribed to a rate-controlling process occurring at a phase boundary [21]. The transition from parabolic to linear kinetics at 615°C implies that a protective layer was not formed or was disrupted as temperature increased. Although a detailed analysis of kinetic models is beyond the scope of this report, some reasonable speculations can be made concerning the underlying causes.

In the case of parabolic kinetics, it seems likely that the inner, mixed spinel layer (see Figs. 1a and 4a) is the protective layer. The composition and microstructure of the oxide layers formed in nitrate melts resemble the duplex oxide layer formed on 316SS and other austenitic Fe-Ni-Cr alloys in steam at similar temperatures [22,23]. A comparison of the oxide scale growth measured in molten nitrate salt with the extensive data concerning oxidation in steam revieved by Armitt, et al, [22] indicates a somewhat slower corrosion rate in salt. A similar comparison between the oxidation rate of 304SS in molten salt and steam has been made by Tortorelli and DeVan [4]. In the case of steam, diffusion in the inner spinel layer is thought to be rate-controlling [22], although it is uncertain if diffusion of oxygen or iron controls. A similar conclusion seems warranted for molten salt. The outer spinel layer is apparently unprotective and likely contains microscopic porosity which is filled with salt. Cr obviously diffuses through the layer, but was not detected in the EMPA scans shown in Fig. 2. The aqueous polishing process used to prepare metallographic samples would remove any evidence of salt however.

The fact that Cr depletion kinetics were parabolic at 605°C suggests that a diffusional process related to that for oxide growth was rate-controlling. One possibility would be diffusion of Cr^{+3} through the mixed spinel layer. However, diffusion control in the spinel layer would be expected to yield a uniform gradient of Cr concentration which decreased in the outward direction, assuming a steady state was attained. The EMPA

plot for Alloy 800, shown in Figure 2, does not indicate such a gradient across the entire inner spinel layer. Other possible rate-controlling processes, such as diffusion of Cr through micropores in the outer spinel layer, cannot be excluded by the EMPA and metallographic analyses.

The occurrence of linear kinetics at 615°C and 630°C implies that both corrosion and depletion rates are controlled by reactions at a phase boundary. It is apparent from the distribution of alloying elements that several oxidation reactions must occur within the corrosion product layer to yield the complex morphology observed. A likely site for several of these reactions to occur is at the boundary between the mixed spinel layer and the sodium ferrate layer since this interface separates phases which contain Cr and Ni from those that do not.

An observation that appears to be significant in understanding the change in corrosion behavior as temperature increases is that NiO was detected at the outer surface of the scale layer at high temperature, but not at 605°C. Like Cr, Ni was not found in the $NaFeO_2$ layer by EMPA (see Figure 4), which means that it must be removed from the spinel layer, transported through the ferrate layer and precipitated at the outer surface. Such a sequence of events is consistent with the phase diagram for Na_2NiO_2 and NiO shown in Figure 6 since the stability boundary lies close to the equilibrium point of the bulk melt. Given that the ferrate layer is microscopically porous, a reduction in the oxygen activity at the inner surface of the ferrate layer, due to its consumption by a variety of reactions, would stabilize sodium nickelate. The nickelate ion, NiO_2^{-2}, could diffuse outward through the salt-filled micropores. At the outer surface, replenishment of oxygen by the atmosphere in contact with the melt would establish an oxygen activity at which NiO is stable, and the oxide would precipitate due to its insolublity.

Similarily, changes in the equilibria of molten salt which penetrated into the scale layer could increase the activity of nitrogen sufficiently to enable internal CrN to form. The process by which CrN could form is analogous to that described for hot corrosion phenomena in molten sulfate deposits, which produce internal sulfides. This topic has been thoroughly

revieved in the literature [24]. In a molten nitrate salt, a decrease in oxygen activity below the atmospheric value could result in formation of nitrite from nitrate, which could subsequently yield nitrogen according to

(6) $$2\ NaNO_2 = Na_2O + N_2 + 3/2\ O_2$$

The nitrogen would then have to diffuse through the M_2O_3 layer to a region of the alloy where CrN is stable according to Figure 5.

Depletion of Cr from the alloy likely occurs by a process similar to that described above for Ni. At the interface between the spinel and ferrate layers, a reaction of trivalent Cr in the oxide layer with oxide or peroxide ions from the salt present locally would result in a basic fluxing process yielding chromate ion. As the phase diagram in Figure 6 shows, sodium chromate is stable over a broad range of oxygen activities, and since it is soluble in the bulk melt [16], it would continuously diffuse through the microchannels in the ferrate layer.

In view of the preceding discussion, the observation that chromium depletion kinetics and oxidation kinetics are linear at 615°C and 630°C suggests that interfacial reactions of the alloy constituents with oxide ion species present in sub-surface molten salt are the rate-controlling processes. This argument is supported by calculations which show a rapid increase of the equilibrium concentration of peroxide in molten nitrate salt as the temperature increases in the range studied here. In the case of Cr depletion, it is quite reasonable to envision linear kinetics associated with the continuous recession into the alloy of a plane at which the Cr concentration in the corrosion products is essentially zero. The effect of the reactions postulated above on the protective nature of the sub-surface oxide layers is not directly evident from the results of microstructural analysis. It is quite possible that the defects created in the sub-surface metal oxide layers by oxide ions from the melt may be too subtle to be resolved by the techniques available. The situation appears analogous to that of molten sulfate-induced hot corrosion.

Summary

The corrosion behavior of two iron-nickel-chromium alloys, Alloy 800 and 316SS, was studied in a molten sodium nitrate-potassium nitrate mixture at temperatures of 605°C to 630°C. A transition in the type of oxidation products formed and the kinetic equations which governed growth of surface oxide layers was observed as temperature increased. At 605°C, oxidation proceeded by parabolic kinetics with the formation of protective spinel oxide layers. At higher temperatures, oxidation displayed linear kinetics and corrosion morphologies were quite complicated, consisting of sodium ferrate, several oxide layers and internal nitridation. At 630°C, the metal loss rate observed for Alloy 800 was 75 microns/year (about 3 mils/year), while that for 316SS was about 100 microns/year. The dependence of corrosion behavior on temperature established that 600°C should be regarded as the upper temperature limit for operating solar central receivers using these alloys.

Chromium was oxidized to form chromate and dissolved in the melt. The presence of dissolved Cr provided a useful diagnostic tool for detecting the transition in corrosion behavior with increasing temperature, since chromium depletion kinetics also changed from a parabolic to a linear rate law as the temperature increased. Depletion of chromium occurred via a basic fluxing process that was accelerated at the higher temperatures at which peroxide ion content increased substantially.

Thermochemical equilibrium calculations have shown that peroxide ion is stable in the molten nitrate salt and that its concentration increases rapidly above 600°C. This report demonstrated that thermochemical analysis of the interactions of metal oxides, derived from the alloying elements, and the molten salt could explain many features of the corrosion process, including the complex organization of oxidation products observed at temperatures above 615°C.

References

1. R.W. Carling and R.W. Mar, "Industrial Use of Molten Nitrate-Nitrite Salts", Sandia National Laboratories, SAND81-8020, Dec. 1981

2. "Advanced Central Receiver Power Station, Phase II", Martin-Marietta Corp., MCR81-1707, Contract Sandia 18-6879C, May 1981.

3. R.W. Bradshaw, in Corrosion in Solar Energy Systems, Symp. Proc. Vol. 83-1, p. 415, The Electrochemical Society, 1983

4. P.F. Tortorelli and J.H. DeVan, "Thermal Convection Loop Study of the Corrosion of Fe-Ni-Cr Alloys by Molten $NaNO_3$-KNO_3", Oak Ridge National Laboratory, TM-8298, Dec. 1982

5. D.R. Boehme and R.W. Bradshaw, High Temp. Sci.,11(8),39(1984)

6. J.W. Slusser, et al, J. Metals, p. 26, July 1985

7. D.C. Erickson, "Air Separation by the Moltox Process, Final Report", Energy Concepts Co., DOE/CS/40287-T2, Feb. 1983

8. D.A. Nissen and D.E. Meeker, Inorg. Chem.,122,716(1983)

9. A.S. Nagelberg and R.W. Mar, in High Temperature Materials, Symp. Proc. Vol. 82-1, p. 89, The Electrochemical Society, 1982

10. A. Rahmel, in Molten Salt Technology, Plenum Press, p.265, 1982

11. H. Fernandez, J.M. Carter and R.A. Osteryoung, in Molten Salts, Symp. Proc. Vol. 84-2, p. 468, The Electrochemical Society, 1984

12. B.J. Brough, D.H. Kerridge and S.A. Tariq, Inorg. Chim. Acta, 11,267(1967)

13. R.N. Kust, Inorg. Chem.,16,2239(1967)

14. F.R. Duke and M.L. Iverson, J. Amer. Chem. Soc.,180,5061(1958)

15. A.M. Shams El Din and E.E. El Hosary, Electrochim. Acta, 13,135(1968)

16. Phase Diagrams for Ceramists, E.M. Levin, C.R. Robbins and H.F. McMordie, editors., Am. Ceram. Soc., 1969 Supplement.

17. I. Barin and O. Knacke, Thermochemical Properties of Inorganic Substances, Springer-Verlag, 1973

18. D. P. Whittle, in Environmental Degradation of High Temperature Materials, Inst. Metall. (U.K.), Series 3, no. 13, Vol.1, 1, 1980

19. D. M. Mathews and R. F. Kruh, Ind. Engg. Chem.,149(1),55(1957)

20. R. W. Bradshaw, "A Thermal Convection Loop Study of Corrosion of Alloy 800 in Molten $NaNO_3$-KNO_3", Sandia National Laboratories, SAND82-8911, Jan. 1983

21. K. H. Hauffe and S. R. Morrison, in High Temperature Gas-Metal Reactions in Mixed Environments, T.M.S.-A.I.M.E., p. 33, 1973

22. J. Armitt, et al, "The Spalling of Steam Grown Oxide from Superheater and Reheater Tube Steels", Electric Power Research Institute, FB-686, p. 2-12, Feb. 1978

23. H. F. Bittner, et al, Met. Trans. A,111,783(1980)

24. J. Stringer, in High Temperature Corrosion in Energy Systems, T.M.S.-A.I.M.E., p. 3, 1985

UNLIMITED RELEASE

INITIAL DISTRIBUTION

U. S. Department of Energy
Solar Thermal Technology Division
Forrestal Bldg., Room 5H021 (CE-314)
1000 Independence Avenue, S.W.
Washington, DC 20585
Attn.: S. Gronich

U. S. Department of Energy
Industrial Programs Division
Forrestal Bldg., Room 5F034 (CE-142)
1000 Independence Avenue, S.W.
Washington, DC 20585
Attn.: R. G. Massey

U. S. Department of Energy
1333 Broadway
Oakland, CA 94612
Attn.: R. Hughey

Air Products and Chemicals, Inc. (2)
TSC R&D Department
P.O. Box 538
Allentown, PA 18104
Attn.: B. R. Dunbobbin
J. W. Slusser

Arizona Public Service
P. O. Box 21666
Phoenix, AZ 85036
Attn.: E. R. Weber

Babcock & Wilcox
Nuclear Equipment Division
P. O. Box 271
Barberton, OH 44203-0271
Attn: D. B. Young

Bechtel National, Inc.
P. O. Box 3965
San Francisco, CA 94119
Attn.: P. DeLaquil

Electric Power Research Institute (2)
Page Mill Road
Palo Alto, CA 94303
Attn.: E. DeMeo
EPRI Library

Foster Wheeler Energy Applications
Dept. C-176
110 South Orange Avenue
Livingston, NJ 07039
Attn.: T. P. Staed, Jr.

Institute of Gas Technology
3424 South State St.
Chicago, IL 60616
Attn.: L. G. Marianovski

Martin Marietta Corporation
P. O. Box 179
Denver, CO 80201
Attn.: T. R. Tracey

Oak Ridge National Laboratory
P.O. Box X
Oak Ridge, TN 37830
Attn.: P. F. Tortorelli

Olin Research Center
350 Knotter Drive
Cheshire, CT 06410
Attn.: D. A. Csejka

Pacific Gas and Electric Company (2)
3400 Crow Canyon Road
San Ramon, CA 94526
Attn.: G. Braun
T. Hillesland, Jr.

Rocketdyne Division
Rockwell International Corp.
6633 Canoga Ave.
Canoga Park, CA 91304
Attn.: A. L. Kohl

Solar Energy Research Institute (2)
1617 Cole Blvd.
Golden, CO 80401
Attn.: G. Gross
SERI Library

Southern California Edison
2244 Walnut Grove Road
Rosemead, CA 91770
Attn.: P. Skvarna

O. E. Jones, 20
R. L. Schvoebel, 1800
R. G. Kepler, 1810
R. E. Whan, 1820
M. J. Davis, 1830
R. B. Deigle, 1831
W. B. Jones, 1832
R. J. Eagan, 1840
D. L. Hartley, 6000
D. G. Schueler, 6220
J. V. Otts, 6222
J. T. Holmes, 6226
R. S. Claassen, 8000; Attn: E. E. Ives, 8100
R. J. Detry, 8200
R. C. Wayne, 8400
P. L. Mattern, 8300; Attn: W. Bauer, 8340
J. S. Binkley, 8350
W. J. McLean, 8360
R. W. Rohde, 8310; Attn: J. A. Brooks, 8312
M. W. Peira, 8314
D. L. Lindner, 8315
J. B. Woodard, 8316
L. R. Thorne, 8313
R. W. Bradshaw, 8313 (10)
R. W. Carling, 8351
J. D. Gilson, 8130
A. C. Skinrood, 8133
Publications Division 8265/Library Division 3141
Technical Library Process Division 3141 (3)
P. W. Dean, 8024, for Central Technical Files (3)